

# Sensitive and Reproducible Immunoassay of Multiple Mycotoxins Using Surface-Enhanced Raman Scattering Mapping on 3D Plasmonic Nanopillar Arrays

Xiaokun Wang, Sung-Gyu Park, Juhui Ko, Xiaofei Xiao, Vincenzo Giannini, Stefan A. Maier, Dong-Ho Kim,\* and Jaebum Choo\*

A surface-enhanced Raman scattering-based mapping technique is reported for the highly sensitive and reproducible analysis of multiple mycotoxins. Raman images of three mycotoxins, ochratoxin A (OTA), fumonisin B (FUMB), and aflatoxin B1 (AFB1) are obtained by rapidly scanning the surface-enhanced Raman scattering (SERS) nanotags-anchoring mycotoxins captured on a nanopillar plasmonic substrate. In this system, the decreased gap distance between nanopillars by their leaning effects as well as the multiple hot spots between SERS nanotags and nanopillars greatly enhances the coupling of local plasmonic fields. This strong enhancement effect makes it possible to perform a highly sensitive detection of multiple mycotoxins. In addition, the high uniformity of the densely packed nanopillar substrate minimizes the spot-to-spot fluctuations of the Raman peak intensity in the scanned area when Raman mapping is performed. Consequently, this makes it possible to gain a highly reproducible quantitative analysis of mycotoxins. The limit of detections (LODs) are determined to be 5.09, 5.11, and 6.07  $\text{pg mL}^{-1}$  for OTA, FUMB, and AFB1, and these values are approximately two orders of magnitude more sensitive than those determined by the enzyme-linked immunosorbent assays. It is believed that this SERS-based mapping technique provides a facile tool for the sensitive and reproducible quantification of various biotarget molecules.

aflatoxin, fumonisin, zearalenone, patulin, and deoxynivalenol are the most well-known mycotoxins. They have been known as a key cause of various diseases, such as cancers, mutagenic and teratogenic effects, liver and kidney damage, and birth defects for a wide range of susceptible animal species including humans.<sup>[1]</sup> In many cases, these diseases are occurred after consumption of grains containing mycotoxins or products made from such grains. Consequently, the presence of mycotoxins in human and animal food supplies is recognized to be a serious health issue. Due to these reasons, mycotoxins are categorized as possible human carcinogens by the International Agency for Research on Cancer.<sup>[2]</sup> Therefore, it is important to develop a rapid and sensitive detection methods for monitoring trace amount of multiple mycotoxins.

To date, various analytical methods, including chromatography, genetic analysis for toxigenic fungus, and enzyme-linked immunosorbent assay (ELISA) have been extensively used for the detection of mycotoxins.<sup>[3,4]</sup> Chromatography

## 1. Introduction

Mycotoxins are secondary metabolites produced by fungi, and they contaminate various agricultural commodities under favorable humidity and temperature conditions. Ochratoxin,

methods include high performance liquid chromatography,<sup>[5]</sup> liquid chromatography-mass spectrometry (LC-MS),<sup>[6]</sup> and gas chromatography-mass spectrometry (GC-MS).<sup>[7]</sup> In GC-MS, the derivatization of liquid sample is needed before analysis. Therefore, LC-MS is a prevalent method for the detection of multiple

X. Wang, Dr. J. Ko, Prof. J. Choo  
Department of Bionano Engineering  
Hanyang University  
Ansan 15588, South Korea  
E-mail: jbchoo@hanyang.ac.kr

Dr. S.-G. Park, Dr. D.-H. Kim  
Advanced Nano-Surface Department  
Korea Institute of Materials Science (KIMS)  
Changwon 51508, South Korea  
E-mail: dhkim2@kims.re.kr

 The ORCID identification number(s) for the author(s) of this article can be found under <https://doi.org/10.1002/smll.201801623>.

DOI: 10.1002/smll.201801623

X. Xiao, Dr. V. Giannini, Prof. S. A. Maier  
The Blakett Laboratory, Department of Physics  
Imperial College London  
London SW7 2AZ, UK

Dr. V. Giannini  
Instituto de Estructura de la Materia (IEM-CSIC)  
Consejo Superior de Investigaciones Científicas  
Madrid 28006, Spain

Prof. S. A. Maier  
Chair in Hybrid Nanosystems  
Nanoinstitut München  
Fakultät für Physik  
Ludwig-Maximilians-Universität München  
München 80539, Germany

mycotoxins. However, it requires multiple bioassay steps, skilled operators and expensive equipment. Genetic analyses such as polymerase chain reaction or DNA microarray have been also applied for the detection of mycotoxin genes in foods.<sup>[1,2]</sup> Unlike bacterial toxins, however, fungal toxins are encoded by multiring structural genes which lack absolute specificity for mycotoxins produced by fungi. Therefore, it has some technical problems to apply this technique for mycotoxin analysis in many cases. Due to the high specificity, reproducibility, and reliability, ELISA has been one of the most useful tools for immunoassay. However, the conventional ELISA method using a 96 well plate format has some technical limitations including poor detection limits, limited multiplex detection capabilities, slow detection speeds, and large sample volumes. Therefore, it is still urgent to develop a sensitive and rapid analytical method for the detection of multiplex mycotoxins.

In recent years, the surface-enhanced Raman scattering (SERS)-based immunoassay using functional metal nanoparticles has garnered much attention due to its high sensitivity and multiplex detection capability.<sup>[8–10]</sup> When SERS nanotags (metal nanoparticles labelled with Raman reporter molecules) are exposed to a laser light source, the incident field is dramatically enhanced at active sites known as electromagnetic “hot spots” by localized surface plasmon effects.<sup>[11–15]</sup> The enhancement effect of Raman signals has overcome the problems of low sensitivity inherent to conventional Raman or fluorescence-based detection techniques.<sup>[16]</sup> Furthermore, multiplex detection is more favorable since Raman peak is much narrower than fluorescence emission band.<sup>[17,18]</sup> However, a reproducibility issue caused by the heterogeneous distribution of hot spots of a plasmonic substrate platform impeded the application of SERS technique for quantitative analysis of target molecules. In the case of 2D plasmonic substrate, the final Raman intensity value was determined by averaging randomly selected multiple detection points (10–20) but this is not enough for determining a final value. Recently, Raman imaging technique through the fast mapping of all pixel points was developed for the reliable quantification of specific target molecules on a plasmonic

substrate.<sup>[19–23]</sup> Average ensemble effects by averaging all randomly distributed hot spots on the substrate made this SERS mapping technique possible to realize a reliable quantification of target molecules.<sup>[24,25]</sup>

In the present study, we report a new analytical method for the sensitive and highly reproducible detection of multiplex mycotoxins using a Raman mapping method. Quantitative analyses of ochratoxin A (OTA), aflatoxin B1 (AFB1), and fumonisin B (FUMB) were performed using the SERS-based imaging method. These are most prominent mycotoxins that found in our agricultural products, such as cereal grains, fruits, and nuts. To overcome the reproducibility issue in SERS-based molecular quantification described above, a large area mapping of SERS nanotags-anchoring mycotoxins on 3D gold nanopillar substrate was investigated. First, two different types of Au nanopillar substrates were fabricated by the sputtering and thermal evaporation methods, and their reproducibility performances were compared with each other. Second, competitive immunoassays using antibody-conjugated SERS nanotags and 3D gold nanopillar substrates were performed for three mycotoxins. Finally, the Raman mapping on 3D substrate was performed for the quantitative evaluation of three mycotoxins. The high uniformity of the densely packed 3D nanopillars over the substrate minimizes spot-to-spot variations of the Raman signal intensity in a scanning area when Raman mapping is performed. We believe that our SERS-based imaging method overcomes the technical limitations such as detection sensitivity and portability in conventional LC-MS and ELISA methods.

## 2. Results and Discussion

### 2.1. Fabrication and Characterizations of 3D Nanopillar Arrays

To find a suitable SERS substrate for the sensitive and reproducible immunoassays of mycotoxins, two different types of Au nanopillar substrates were fabricated in this work. **Figure 1a** displays schematic illustrations for the fabrication of 3D nanopillar

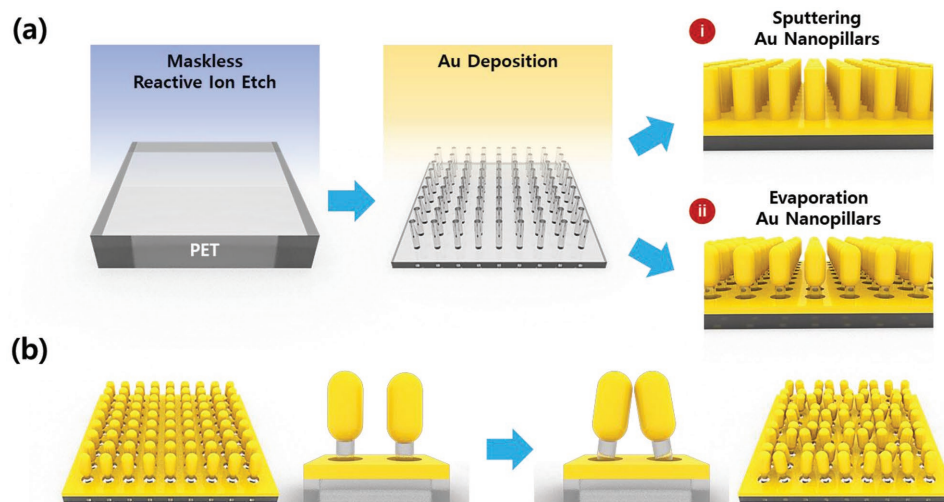


**Figure 1.** Schematic illustrations for a) the fabrication of 3D nanopillar substrates by i) sputtering and ii) thermal evaporation methods. b) Leaning effects of adjacent nanopillars after solution evaporation.

arrays by two different coating methods; one is a sputtering technique and the other is a thermal evaporation method. Both coating technologies can be tuned to achieve different properties of coated films. First, polyethylene terephthalate (PET) surfaces were treated with maskless Ar plasma to generate a high areal density of polymer nanopillars.<sup>[26,27]</sup> Figure S1a,b in the Supporting Information shows the scanning electron microscope (SEM) images of a flat (reactive ion etching (RIE) = 0 s) and a nanopillar PET substrate (RIE = 120 s) along the RIE time, respectively. In Figure S1b in the Supporting Information, the average areal density of the PET nanopillar substrate was estimated to be 80 number  $\mu\text{m}^{-2}$ , and the aspect ratio of each nanopillar was 6.3. Onto this PET nanopillar substrate, Au was deposited by the sputtering or thermal evaporation method to fabricate 80 nm thick gold nanopillar structures. A patterned large area ( $4 \times 4 \text{ cm}^2$ ) plasmonic substrate, with a pattern of 49 circles ( $7 \times 7$  wells, each well is enclosed with Au nanopillars), was also fabricated for the immunoassay of multiple mycotoxins. These nonlithographic techniques are cost-effective and high throughput methods over other lithography processes for fabricating wafer-scale plasmonic substrates.

Figure 2 shows SEM images of Au/PET nanopillar arrays fabricated by Au sputtering and evaporation methods. The sputtering substrate does not show any significant change after water evaporation because of the rigid property of pillars (Figure 2a,c). On the other hand, surface tension causes the leaning effects of two or three adjacent nanopillars and they induce the self-assembly of hot spots during the evaporation process (Figure 1b, Figure 2b,d). This leaning effect decreases a gap distance between nanopillars and greatly enhances the coupling of local plasmonic fields. Consequently, the Raman intensity of the evaporation substrate is much stronger than that of the sputtering substrate since it retains nano gaps necessary to form hot junctions.

Another important issue in SERS substrates is the uniformity of 3D nanostructures to achieve reproducible Raman signals of target mycotoxins. To investigate the uniformity

across the substrate, 3D Raman mapping images for the sputtering and evaporation substrates were measured and analyzed in Figure 3a. Here,  $10^{-6} \text{ M}$  malachite green isothiocyanate (MGITC) solution was dropped onto sputter and evaporation substrates respectively, and their Raman peak intensity variation at  $1617 \text{ cm}^{-1}$  was used for Raman mapping. An  $x$ - $y$  translational stage was used for scanning a  $50 \mu\text{m} \times 50 \mu\text{m}$  steps over a  $2100 \mu\text{m}$  ( $x$ -axis) and  $2100 \mu\text{m}$  ( $y$ -axis) range by the computer control. Consequently, total 1849 pixels (1 pixel =  $50 \mu\text{m} \times 50 \mu\text{m}$ ) were obtained for the square area and 1368 pixel points were imaged for the round circle area of each substrate. The accumulation number and exposure time for each pixel were 1 and 0.1 s, respectively. As shown in this figure, the sputtering substrate i) shows a serious nonuniform intensity distribution due to the following reasons. First, a metal shadow mask (panel (i) in Figure 3b) was used in Au deposition for the formation of array patterns in the sputtering process. During the deposition process, it is difficult to completely attach this shadow mask on the substrate surface, and the gap between the substrate and the mask causes a serious shadowing effect. Second, the sputter gun was positioned with  $\approx 45^\circ$  angle as shown in the layout of the deposition system in Figure S2 in the Supporting Information. Herein, the sputter source was positioned on the opposite side of the substrate. Therefore, the deposition thickness for close side from the gun was different from that for far side even though the substrate was continuously rotated during the deposition. As a result, a thickness gradient was observed on the sputtering substrate. On the other hand, a relatively uniform Raman intensity distribution was observed for the evaporation substrate (panel (ii) in Figure 3a). Our experimental results indicate that Raman imaging method is useful for the uniformity evaluation of 3D nanopillar plasmonic substrates. SERS signal intensity measured at the leaned plasmonic nanostructures (fabricated by evaporation method) was 6.2 times stronger than the signal intensity measured at the nonleaning plasmonic nanostructures (fabricated by sputtering method). On the basis of these

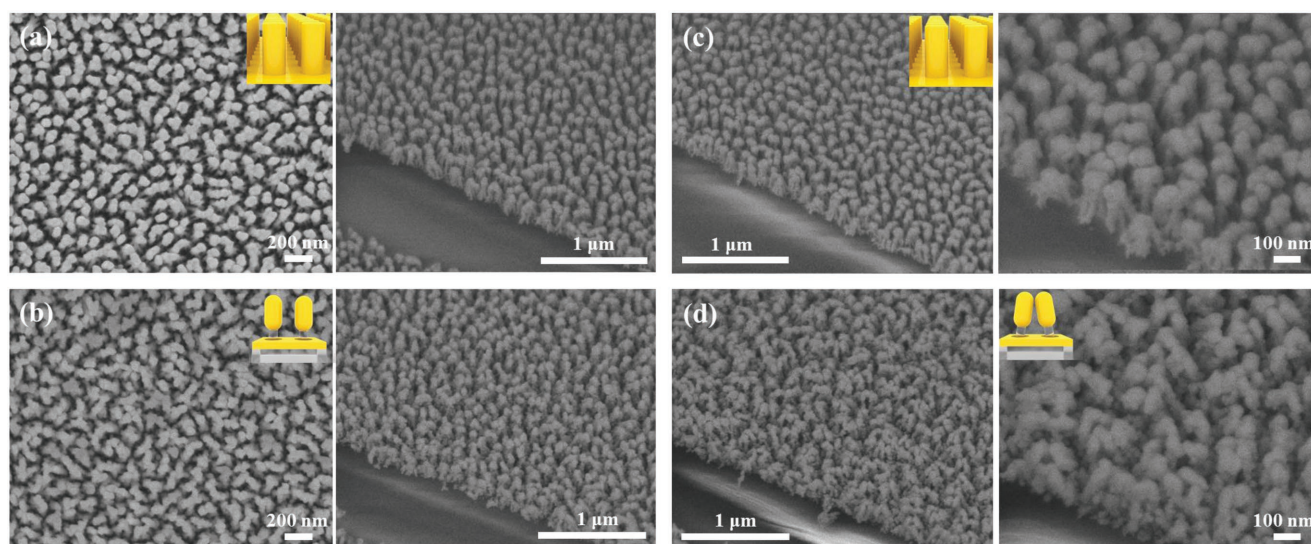


**Figure 2.** SEM images of a) sputtering and b) thermal evaporation substrates before water evaporation. SEM images of c) sputtering and d) thermal evaporation substrates after water evaporation.

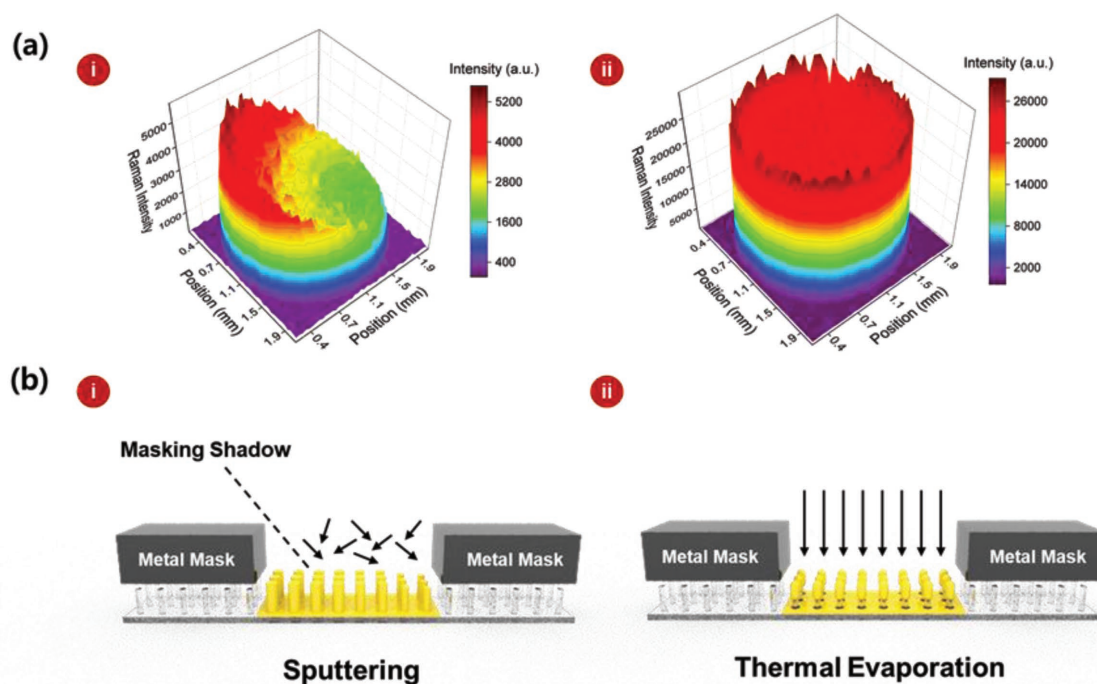


**Figure 3.** a) 3D representation of the Raman mapping images of  $10^{-6}$  M MGITC for i) sputtering and ii) evaporation substrates. An  $x$ - $y$  translational stage was used for scanning  $50 \mu\text{m} \times 50 \mu\text{m}$  steps over a  $2100 \mu\text{m}$  ( $x$ -axis) and  $2100 \mu\text{m}$  ( $y$ -axis) range by the computer control. Total 1849 pixels (1 pixel =  $50 \mu\text{m} \times 50 \mu\text{m}$ ) were obtained for the square area and 1368 pixel points were imaged for the round circle area of each substrate. The scale bar on the right displays the color decoding for different Raman intensities. b) Au deposition processes on i) sputtering and ii) evaporation substrates. A 0.25 mm thick metal shadow mask was used for the sputtering substrate.

Raman mapping images, it is concluded that 3D Au nanopillar substrate, fabricated by the evaporation coating method, is more suitable for the reproducible measurement, and it was used as a SERS assay template for the quantitative evaluation of multiple mycotoxins in this work. Energy-dispersive X-ray spectroscopy was also used for evaluation of the chemical composition of the nanostructures (Figure S3, Supporting Information). Elemental analysis of the Au/PET nanopillar substrate shows a composition of Au (28.2%), C (64.8%), and O (7.0%). Herein, spectral peaks for C and O were also observed since X-rays with an accelerating voltage of 15 kV could penetrate into the PET nanopillar surface.

Additionally, the reproducibility of seven different round-shape wells was tested to confirm their feasibility for the multiplex assay of various mycotoxins. For this purpose,  $10^{-6}$  M MGITC solution was dropped onto seven different wells and their Raman mapping images at  $1617 \text{ cm}^{-1}$  were measured and analyzed as shown in Figure 4a. Here, the uniform distributions of light yellow color for all the wells demonstrate that the well-to-well reproducibility is consistent. Raman spectra taken from 50 randomly selected points in well #1 and the distribution of Raman peak intensity at  $1617 \text{ cm}^{-1}$  for all the seven wells were displayed in Figure 4b,c, respectively. According to our statistical analysis, the relative standard deviation (RSD) for seven wells was as low as 5.7%, and this low RSD indicates that the well-to-well variation in SERS intensity is very low. The RSD of 3D Au nanopillar substrate, fabricated by the sputtering method, was estimated to

be 17.2% (Figure S4, Supporting Information). On the basis of these experimental data, it is concluded that these 3D Au nanopillar microarray wells, fabricated by the evaporation method, are suitable for the quantitative analysis of multiple mycotoxins.

To evaluate the limit of detection (LOD) of MGITC molecules adsorbed on the evaporation substrate,  $1 \mu\text{L}$  of MGITC was dropped onto Au nanopillar well. After the evaporation of solvent, Raman spectra of MGITC were measured from ten randomly selected points in each microarray well. Figure S5a in the Supporting Information shows the Raman spectra of MGITC on 3D Au nanopillar substrate in the  $0$ – $10^{-6}$  M range. Figure S5b in the Supporting Information displays a linear relationship in the concentration range from  $10^{-9}$  M to  $10^{-6}$  M. LOD was estimated to be  $7.39 \times 10^{-10}$  M based on three standard deviations from the background. This low LOD value indicates that 3D gold substrate exhibits a superior detection sensitivity over other substrates. As described above, the surface tension leads nanopillars to lean toward each other after solvent evaporation in the evaporation substrate. Figure S6 in the Supporting Information shows SEM images of the substrate a) before and b) after solvent evaporation. As shown in this figure, two or three adjacent nanopillars have leaned toward nearest neighbors during the solvent evaporation process. Consequently, the coupling of local plasmonic fields is greatly enhanced due to the decrease of the gap distance.

The average enhancement factor (EF) for 3D nanopillar substrate was also determined from the Raman data

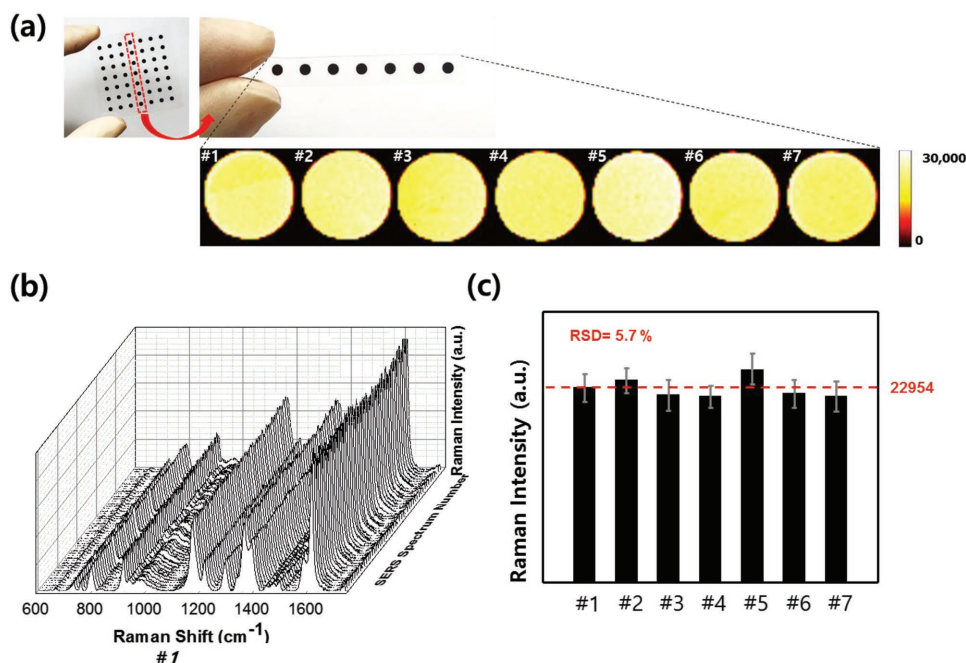


**Figure 4.** a) Digital photograph of  $7 \times 7$  microarray wells (top). SERS mapping images were acquired using peak intensity at  $1617 \text{ cm}^{-1}$  for seven parallel (#1–#7) circular wells labeled with  $10^{-6} \text{ M}$  MGITC (bottom). The scale bar on the right displays the color coding for different Raman intensities. b) Raman spectra taken from 50 randomly selected points in well #1. c) Distributions of average Raman peak intensity at  $1617 \text{ cm}^{-1}$  for seven circular wells. The RSD for seven wells was calculated to be 5.7%.

in Figure S5c in the Supporting Information. A droplet of  $1 \times 10^{-9} \text{ M}$  MGITC solution was dropped on the surface of 3D nanopillar substrate, and the droplet was allowed to evaporate. Here, the surface area was measured to be  $0.785 \text{ mm}^2$ , and we assumed that MGITC molecules are evenly distributed across the surface area. From the center of the dried area, its Raman intensity was ( $I_{\text{SERS}}$ ) was measured using a  $20 \times$  objective and  $632.8 \text{ nm}$  laser with a power of 10%. To establish the reference value ( $I_{\text{Ref}}$ ), 2D glass substrate was used as a reference. A droplet of MGITC with a concentration of  $5.0 \times 10^{-3} \text{ M}$  was dropped again on the 2D glass substrate surface, and the droplet was allowed to evaporate. Then its Raman intensity was measured under the same conditions, and the enhancement factor was determined by the following Equation (1).<sup>[28,29]</sup>

$$EF = \frac{I_{\text{SERS}}/N_{\text{SERS}}}{I_{\text{Ref}}/N_{\text{Ref}}} \quad (1)$$

In this equation,  $N = C \cdot V \cdot NA/S$ , where  $C$ ,  $V$ ,  $NA$ , and  $S$  represent the concentration of MGITC solution, the volume of the MGITC solution dropped, Avogadro constant and the area of the MGITC molecules covered, respectively. Both substrates were dried in the air. The foregoing equation thus becomes as following Equation (2).

$$EF = \frac{I_{\text{SERS}}}{I_{\text{Ref}}} \cdot \frac{S_{\text{SERS}} V_{\text{Ref}} C_{\text{Ref}}}{S_{\text{Ref}} V_{\text{SERS}} C_{\text{SERS}}} \quad (2)$$

From this equation, the EF was determined to be  $9.78 \times 10^6$  for the 3D nanopillar substrate.

## 2.2. SERS Imaging-Based Platform for Multiple Detection of Mycotoxins

The final goal in this work is the application of the 3D nanopillar substrate as a SERS–imaging–based platform for the highly sensitive and reproducible immunoassay of multiple mycotoxins. For this purpose, OTA, FUMB, and AFB1 were selected as detection targets for its validation. **Figure 5** demonstrates a sequential process for the immunoassay of mycotoxins. A competitive binding assay using an antibody was performed since all the mycotoxins are small size molecules and have only one binding epitope. First, carboxylic acid self-assembled monolayers were immobilized on 3D nanopillar surface for the formation of hydrophilic surface. Subsequently, the carboxylic acid groups were activated by 1-ethyl-3-(3-(dimethylamino)propyl) carodiimide (EDC) and *N*-hydroxysuccinimide (NHS), and then mycotoxin–bovine serum albumins (BSAs) were immobilized on the substrate in **Figure 5a**. The fabrication process for antibody-conjugated SERS nanotags was displayed in **Figure 5b**. The surface of the MGITC-labelled gold nanoparticles (AuNPs) was modified with dihydroliipoic acid (DHLA) and then activated carboxyl groups were reacted with EDC/NHS solution to immobilize secondary antibodies on the surface of AuNPs.

Antibody conjugation on the surface of AuNPs were identified by measuring transmission electron microscopy (TEM) image, UV–vis absorption spectra, dynamic light scattering (DLS) distribution, and Raman spectra. The average diameter of AuNPs was estimated to be  $\approx 40 \text{ nm}$  from the TEM image in **Figure S7a** in the Supporting Information. UV–vis spectral data demonstrated that the surface plasmon band was

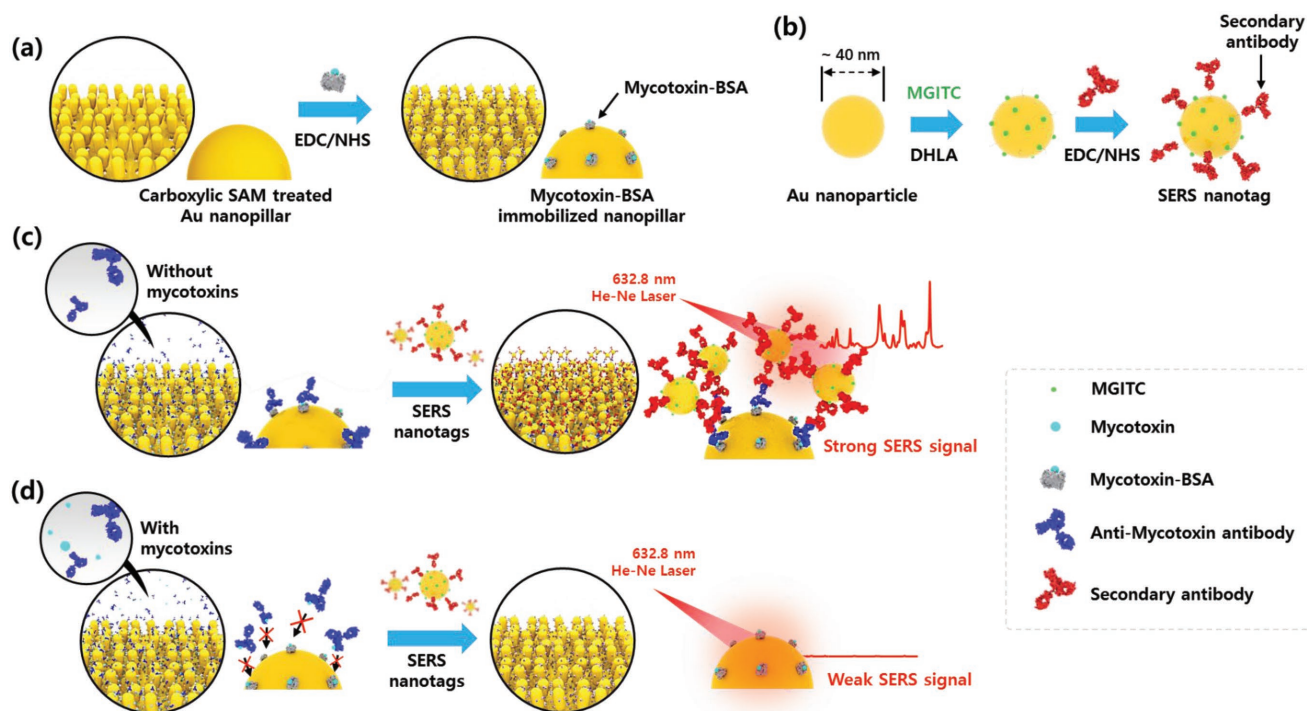


**Figure 5.** Schematic illustration for the sequential process of the immunoassay of mycotoxin. a) Immobilization of mycotoxin-BSAs on 3D plasmonic substrate. b) Fabrication of a secondary antibody-conjugated SERS nanotag. Procedures of competitive immunoassay in the c) absence and d) presence of mycotoxins.

slightly shifted from 529 to 531 nm upon antibody conjugation as shown in Figure S7b in the Supporting Information. The average diameter of AuNPs increased from 40 to 50 nm after antibody conjugations according to the DLS data in Figure S7c in the Supporting Information. These spectral changes in UV-vis spectroscopy and DLS indicate that antibodies were successfully adsorbed on the surface of AuNPs. Raman spectra of AuNPs and SERS nanotags in Figure S7d in the Supporting Information demonstrate that Raman reporter molecules are also successfully adsorbed on the surface of AuNPs.

A schematic illustration of the SERS-based competitive immunoassay process is displayed in Figure 5c,d. In the absence of target mycotoxins, antimycotoxin antibodies are first captured by mycotoxin-BSAs immobilized on 3D substrates by antibody-antigen interactions, and then secondary antibody-conjugated SERS nanotags were captured by the primary antibodies on the surface by antibody-antibody interactions. Consequently, many SERS nanotags are bound onto 3D nanopillar substrate and they form a confined 3D plasmonic field, leading to the increase of Raman signal intensity caused by electromagnetic field enhancement (Figure 5c). In the presence of the target mycotoxins, however, a competitive immunoreaction towards antimycotoxin antibodies is proceeded between target mycotoxins and mycotoxins-BSAs immobilized on the 3D substrate. When antimycotoxin antibodies reacted with target mycotoxins, they cannot be captured the mycotoxins-BSAs immobilized on the 3D nanopillar substrate. As a result, the number of secondary antibody-conjugated SERS nanotags bound onto primary antibodies immobilized on substrate was decreased, and it leads to the decrease of the

Raman signal intensity (Figure 5d). Three lines of microwells on the patterned 3D plasmonic substrate with 49 circle wells (total seven lines and one line includes seven circle wells) were used for the multiplex detection of three mycotoxins as shown in Figure 6a. Figure 6b,c demonstrate SERS mapping and SEM images of the plasmonic substrates in the absence and presence of OTAs. In the absence of target OTAs, it was observed that many SERS nanotags (red circles in Figure 6b) were bound onto the 3D nanopillar substrate, which results in high SERS signal enhancements of MGITC molecules. On the other hand, few SERS nanotags were bound onto the substrate for the high concentration ( $10^6$  pg mL<sup>-1</sup>) of the target OTA (Figure 6c).

We investigated 3D plasmonic coupling effect of SERS nanotag bound onto the leaned Au nanopillars (Figure 6d,e). Each Au nanopillar was assumed to be topped with one large prolate spheroid AuNP with an equatorial diameter of 65 nm and had a distance of 50 nm with nearest Au nanopillar at upright position (before capillary leaning). Then, average gap distance between Au nanopillars was decreased to 6.1 nm by capillary leaning effects (Figure 2d). The antibody-conjugated SERS nanotags with diameter of 50.4 nm was bound onto the leaned Au nanopillars (Figure 6d). A linearly polarized 632.8 nm plane wave illumination beam was directed onto the plasmonic nanostructures with polarization along the dimer axis. The region between the top of leaned Au nanopillars and SERS nanotag showed the highest electric field enhancement. The simulation results confirmed that the hot spot was highly localized at the interface between SERS nanotag and leaned Au nanopillars due to plasmonic coupling effects. Since antibody-conjugated SERS nanotags are comparable to gap

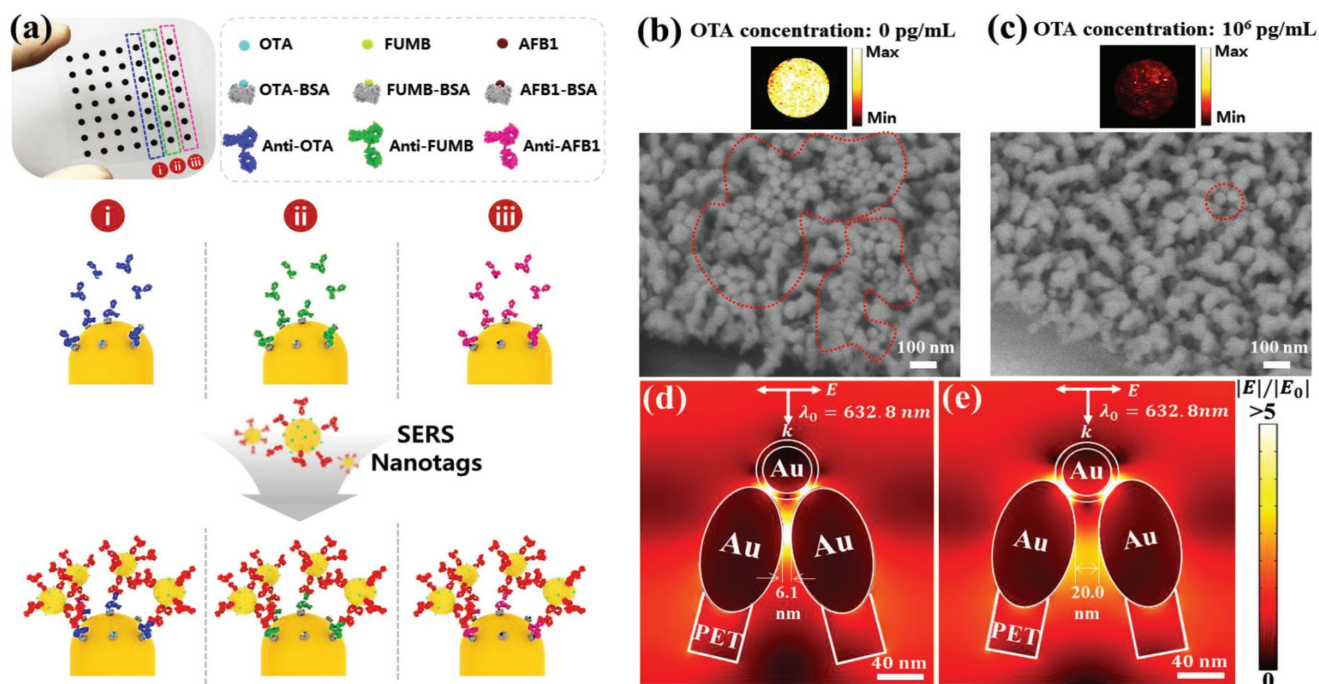


**Figure 6.** a) Digital photograph of  $7 \times 7$  microarray wells and schematic illustration for the competitive immunoassays of OTA, FUMB, and AFB1 on 3D plasmonic substrates. Three lines were used for the multiplex immunoassay of three mycotoxins. SERS mapping and SEM images of SERS nanotags captured by the 3D plasmonic nanopillars on the 3D plasmonic substrates b) without OTA and c) with  $10^6$  pg mL<sup>-1</sup> OTA. Red circles indicate the bounding areas of SERS nanotags with 3D plasmonic nanopillars. Numerical simulation of the electric field distribution over the SERS nanotag-anchoring antibody captured on the leaned Au nanopillars with a gap size of d) 6.1 nm and e) 20.0 nm. A linearly polarized 632.8 nm plane wave illumination beam was directed onto the plasmonic nanostructures with polarization along the dimer axis. The distance between Au nanopillar and antibody-conjugated SERS nanotags was set to 5.2 nm, determined from SEM images and DLS distributions.

size of leaned Au nanopillars (Figure 6e), our Au nanopillar substrate is highly efficient for capturing SERS nanotags, which results in the highly sensitive immunoassays. We also investigated the nonspecific binding of SERS nanotags for the ochratoxin A-conjugated BSA (OTA-BSA) immobilized substrate. As shown in Figure S8 in the Supporting Information, SERS nanotags were successfully bound onto the substrate only in the presence of anti-OTA antibody, and consequently the color of three wells on the top changed to bright yellow color.

As described above, it is not enough to average several detection points to achieve a reproducible quantitative result since it is not easy to consistently control the nanogaps produced by SERS nanotags across the microwell substrate. In

the present work, therefore, a SERS imaging-based assay platform which uses a mapping technique was utilized for a highly reproducible immunoassay of three mycotoxins. Using the computer-controlled  $x$ - $y$  translational stage, 1368 pixels (1 pixel =  $50 \mu\text{m} \times 50 \mu\text{m}$ ) were imaged for all the circle wells, and it takes  $\approx 3.5$  min to obtain a SERS mapping image for each well. With an increase in the mycotoxins concentration from 0 to  $10^6$  pg mL<sup>-1</sup>, fewer SERS nanotags attached to the substrate, leading to the darker imaging color on the substrate. **Figure 7** demonstrates the images measured with the Raman peak intensity at  $1617 \text{ cm}^{-1}$  for various concentrations of three mycotoxins in the  $0$ – $10^6$  pg/mL range. The bar scale on the right shows the color decoding for Raman intensity. When less SERS nanotags bound

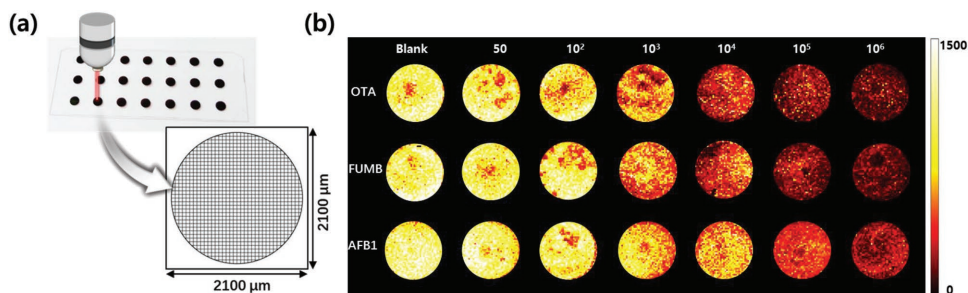


**Figure 7.** a) Detection pixels of a microarray well for the scanning of Raman signals. One pixel is  $50 \mu\text{m} \times 50 \mu\text{m}$ , and 1368 pixel points were imaged for each circular well using a computer-controlled  $x$ - $y$  translational stage. b) SERS mapping images acquired using peak intensity at  $1617 \text{ cm}^{-1}$  for seven different concentrations of OTA, FUMB, and AFB1 in the  $0$ – $10^6$  pg mL<sup>-1</sup> range. The scale bar on the right displays the color coding for different Raman intensities.

onto the nanopillar substrate by primary antibody-secondary antibody interactions from blank to  $10^6$   $\text{pg mL}^{-1}$ , corresponding Raman intensity was decreased because this is a competitive assay. As a result, the SERS nanotags-binding nanopillar arrays got darker with the increase in mycotoxin concentration.

Figure 8 shows the average Raman spectra for 1368 pixel points of the SERS mapping circles in the presence of various mycotoxin concentrations. For OTA, FUMB, and AFB1, the Raman peak intensities concomitantly decrease with the increase of their concentrations. Corresponding calibration curves for OTA, FUMB, and AFB1 are displayed. Here, the error bars indicate standard deviations from three measurements. Their LODs were also determined to be 5.09, 5.11, and  $6.07$   $\text{pg mL}^{-1}$  for OTA (Figure 8a), FUMB (Figure 8b), and AFB1 (Figure 8c), respectively. Each LOD was calculated on the basis of three standard deviations from the blank. In order to evaluate the detection sensitivity of the proposed SERS imaging-based assay, ELISA immunoassays were also performed for OTA, FUMB, and AFB1. Figure S9a in the Supporting Information shows the ELISA assay process using 96-well plate and corresponding ELISA calibration curves for three mycotoxins are displayed in Figure S9b in the Supporting Information. The LODs determined by conventional ELISA were 0.72, 0.70, and  $0.84$   $\text{ng mL}^{-1}$  for OTA, FUMB, and AFB1, respectively. When compared these LODs, the value determined by our SERS imaging-based assay is approximately two orders of magnitude more sensitive than that determined from ELISA. Moreover, our approach consumes small volume of sample ( $0.75$   $\mu\text{L}$ ) and

this amount is at least 70 times smaller than that required in ELISA.

To evaluate the selectivity performance of our SERS imaging-based assay platform, tests were performed for three samples with different mycotoxin ratios. Sample 1 contains  $0$   $\text{pg mL}^{-1}$  of OTA,  $10^4$   $\text{pg mL}^{-1}$  of FUMB,  $10^6$   $\text{pg mL}^{-1}$  of AFB1; sample 2 contains  $10^6$   $\text{pg mL}^{-1}$  of OTA,  $0$   $\text{pg mL}^{-1}$  of FUMB,  $10^4$   $\text{pg mL}^{-1}$  of AFB1; sample 3 contains  $10^4$   $\text{pg mL}^{-1}$  of OTA,  $10^6$   $\text{pg mL}^{-1}$  of FUMB,  $0$   $\text{pg mL}^{-1}$  of AFB1. Corresponding SERS mapping images of three sample mixtures measured for OTA, FUMB, and AFB1 substrates are shown in Figure 9a, their average SERS intensities of 1368 pixels for each well are displayed in Figure 9b. Recovery values corresponding to three cocktail solutions in Figure 9 are also demonstrated in Table S1 in the Supporting Information. The assay results demonstrate that this SERS-based imaging approach shows inherently high selectivity for three different mycotoxin cocktail solution mixtures.

### 3. Conclusion

In the present study, we developed a new quantitative sensing method of three mycotoxins, OTA, AFB1, and FUMB, using a Raman mapping technique of SERS nanotags-anchoring mycotoxins captured on 3D nanopillar plasmonic substrate. Raman signal reproducibility of two different Au/PET nanopillar substrates, fabricated by the sputtering and thermal evaporation methods, was tested. The sputtering substrate demonstrated a

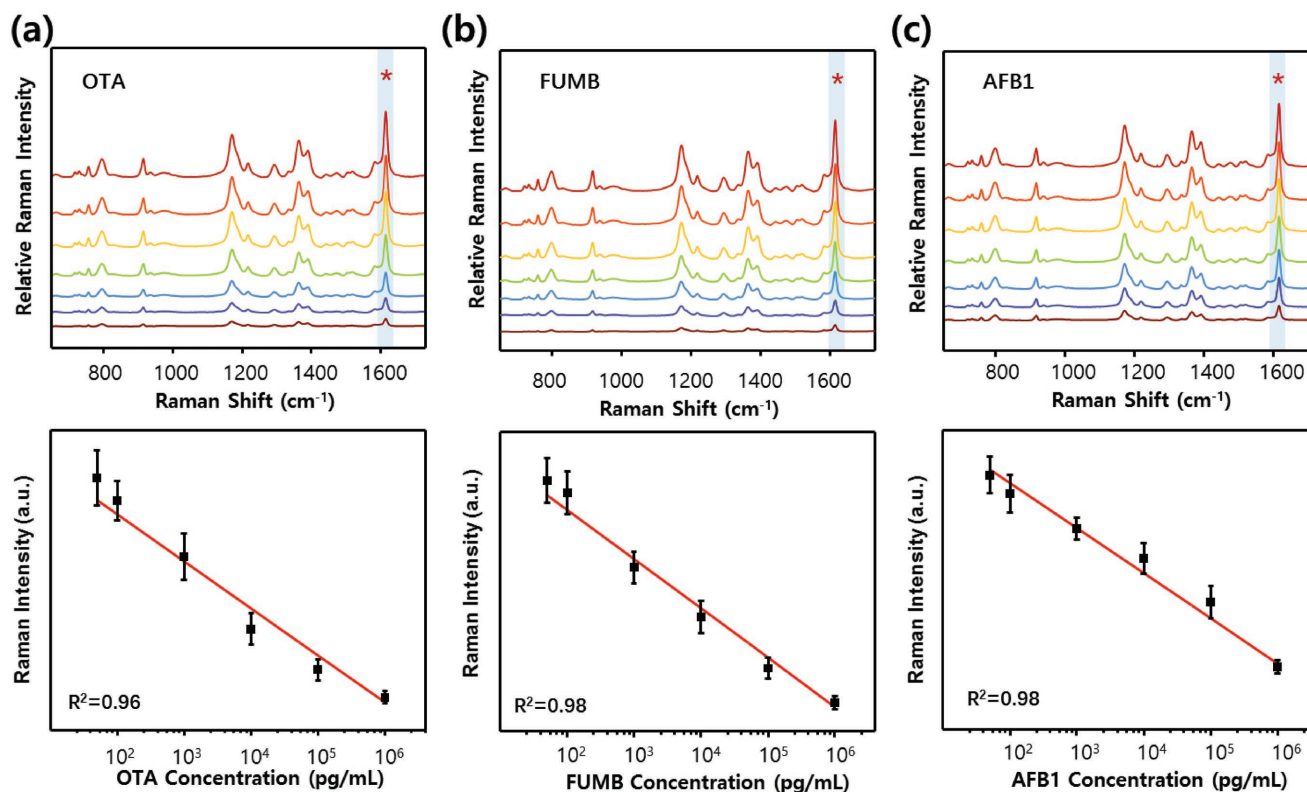
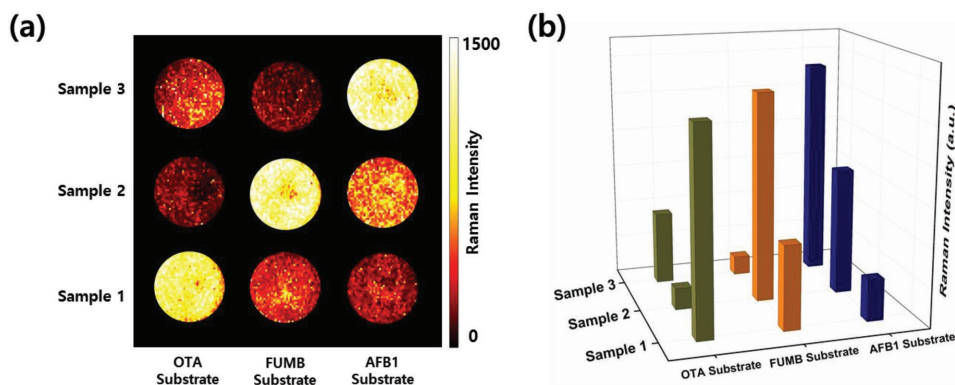


Figure 8. Average SERS spectra of 1368 pixel points for a) OTA, b) FUMB, and c) AFB1 in the  $0$ – $10^6$   $\text{pg mL}^{-1}$  range, and corresponding calibration curves. Semilog scale was used on the x axis. The error bars indicate standard deviations from three measurements.



**Figure 9.** a) SERS mapping images using the peak intensity at  $1617\text{ cm}^{-1}$  for three cocktail solutions including different ratios of three mycotoxins (OTA: FUMB: AFB1, sample 1,  $0:10^4:10^6$ ; sample 2,  $10^6:0:10^4$ ; and sample 3,  $10^4:10^6:0$ ). b) Comparison of average SERS peak intensities at  $1617\text{ cm}^{-1}$  from the SERS mapping images shown in panel (a).

serious nonuniform intensity distribution due to the attachment problem of a metal shadow mask and the tilted position of the sputtering gun. In the case of the evaporation substrate, a uniform Raman intensity distribution was observed, and it also induced a strong Raman enhancement through the capillary leaning effect of Au nanopillars.

Using this 3D evaporation nanopillar substrate together with antibody-conjugated SERS nanotags, competitive immunoassays of three mycotoxins were performed. The high uniformity of the densely packed nanopillars in the 3D plasmonic substrate minimized the spot-to-spot fluctuations of the Raman peak intensity in the scanned area when Raman mapping was performed. Consequently, the Raman mapping made it possible to gain a highly sensitive and reproducible quantitative analysis of a mycotoxin. Additionally, a patterned 3D plasmonic substrate composed of 49 circle wells were fabricated and utilized for the SERS-based competitive assays of multiple mycotoxins. According to the average Raman spectra for 1368 pixel points of SERS mapping circles, the LODs were determined to be 5.09, 5.11, and  $6.07\text{ pg mL}^{-1}$  for OTA, FUMB, and AFB1, and these values are approximately two orders of magnitude more sensitive than those determined by the ELISA assays. Selectivity tests were also performed for three cocktail samples with different mycotoxin ratios, and our SERS mapping-based assay technique demonstrated a good selectivity for OTA, FUMB, and AFB1. Our SERS-based assay results were also compared with the previously reported ones using other detection techniques in Table S2 in the Supporting Information. On the basis of this comparison, it is concluded that this SERS-based mapping approach not only provides a facile detection tool for the quantification of multiple mycotoxins but can also serve as a new multiplex assay platform for other bio-target molecules.

#### 4. Experimental Section

**Materials:** Gold(III) chloride trihydrate (>99.9%), sodium citrate, ethanolamine, DHLA, EDC, NHS, tetrahydrofuran (99%), 11-mercaptoundecanoic acid, 6-mercapto-1-hexanol, BSA, 2-(N-morpholino)ethanesulfonic acid, Tween 20, OTA, AFB1,

FUMB, OTA-BSA, aflatoxin B1-conjugated BSA and antimouse immunoglobulin G were purchased from Sigma-Aldrich (St. Louis, MO, USA). FUMB-BSA was purchased from Creative Diagnostics (New York, NY, USA). Phosphate-buffered saline (PBS) ( $10\times$ , pH 7.4) and MGITC were purchased from Invitrogen Corporation (Carlsbad, CA, USA). Antiochratoxin A monoclonal antibody was purchased from Abcam (Cambridge, MA, USA). Ultrapure water ( $18\text{ M}\Omega\text{-cm}^{-1}$ ) used in this work was obtained from a Milli-Q water purification system (Billerica, MA, USA).

**Instrumentation:** High-magnification TEM images were obtained using a JEOL TEM 2100F instrument (JEOL, Tokyo, Japan) at an accelerating voltage of 200 kV. SEM images were taken by a MIRA3 instrument (TESCAN, Brno, Czech Republic) at an accelerating voltage of 20 kV. DLS data were acquired using a Nano-ZS90 apparatus (Malvern Instruments, Malvern, UK). UV-vis absorption spectra were measured with a Cary 100 spectrophotometer (Varian, Salt Lake City, UT, USA). SERS mapping images were acquired using an inVia Renishaw Raman microscope system (Renishaw, New Mills, UK). ELISA was performed using a PowerWave X340 microplate reader (Winooski, VT, USA) equipped with a 96-well plate. RIEs, including thermal evaporation and sputtering, were performed using a RIE System (SNTek Co. Ltd., Suwon, Korea).

**Preparation of Antibody-Conjugated SERS Nanotags:** AuNPs were prepared according to the previously reported seed growth method<sup>[30]</sup> with a slight modification. Briefly, a solution of  $2.2\times 10^{-3}\text{ M}$  sodium citrate in a three-necked round-bottomed flask was heated under vigorous stirring. As soon as boiling, 0.5 mL of  $25\times 10^{-3}\text{ M}$   $\text{HAuCl}_4$  was added to the flask for the formation of Au seeds. The color of the solution changed from yellow to bluish gray and then to soft pink in 10 min. The reaction was cooled in the same vessel until the temperature of the solution reached  $90\text{ }^\circ\text{C}$ , and then 0.5 mL of  $60\times 10^{-3}\text{ M}$  sodium citrate and 0.5 mL of  $25\times 10^{-3}\text{ M}$   $\text{HAuCl}_4$  were sequentially added (every 2 min). This process was repeated 12 times, and the resultant solution was stirred 30 min at  $90\text{ }^\circ\text{C}$ . TEM, UV-vis spectrophotometer and DLS were used to characterize the morphology and size distribution of AuNPs. A sequential procedure for the immobilization of Raman reporter molecules on the surface of AuNPs was reported elsewhere. 0.5  $\mu\text{L}$  of  $10^{-4}\text{ M}$  MGITC was added to 1 mL of  $0.1\times 10^{-9}\text{ M}$  AuNPs. The MGITC-AuNPs mixture was reacted for 30 min under gently stirring. Immobilization of MGITC on the surface of AuNPs was identified by SERS measurements.

Antibody conjugation on the surface of AuNPs was initiated by the addition of 5  $\mu\text{L}$  of  $0.1\times 10^{-3}\text{ M}$  DHLA. Two -SH functional groups of DHLA were cleaved and covalently bonded to the surface of AuNPs. The solution was incubated for 2 h and then unreacted chemical reagents were removed by centrifugation. The -COOH terminal groups on the surfaces of AuNPs were activated by adding

5  $\mu\text{L}$  of  $2 \times 10^{-3}$  M EDC and NHS. After 40 min, 0.5  $\mu\text{L}$  of 1 mg  $\text{mL}^{-1}$  secondary antibodies were reacted with the solution for 2 h at room temperature. Finally, unreacted sites on the surfaces of the Au NPs were deactivated by 2  $\mu\text{L}$  of  $1 \times 10^{-3}$  M ethanolamine for 30 min. Nonspecific binding chemicals and antibodies were washed out through centrifugation twice, and the remaining SERS nanotags was suspended in PBS solution.

**Fabrication of Au/PET Nanopillar Substrates:** A PET polymer substrate with a thickness of 125  $\mu\text{m}$  was purchased from Panac Inc. and was used without any modification. Ar plasma treatment of the polymer substrate was performed using a custom-built 13.56 MHz RF ion etching instrument. The inlet Ar flow rate and the working pressure were fixed at three standard cubic centimeters per minute (scm) and 32 mTorr during Ar plasma treatment for 2 min. The plasma power was 100 W. A shadow mask pattern comprising a circular hole with a diameter of 2 mm and a period of 6 mm was designed. A shadow mask array was then firmly attached to the PET film after Ar plasma treatment. 80 nm thick Au/PET nanostructures were directly deposited on the PET nanopillars using a sputtering or a thermal evaporation system with a deposition rate of  $2.0 \text{ \AA s}^{-1}$ . Base pressure of the chamber was  $9.6 \times 10^{-6}$  Torr.

**SERS-Based Competitive Immunoassay:** For the immunoassay, 0.75  $\mu\text{L}$  of mycotoxin and 0.75  $\mu\text{L}$  of antimycotoxin antibody were dropped on the mycotoxin-BSA immobilized substrate and incubated for 1 h in a humid chamber. The substrate was washed three times with PBS solution. Subsequently, 1.5  $\mu\text{L}$  SERS tags was dropped on the substrate, incubated for another 1 h in a humid chamber, and then washed three times with PBS solution. The substrate was dried in oven at 37  $^{\circ}\text{C}$  before measurement.

SERS mapping images were acquired using an inVia Renishaw Raman microscope system; a He-Ne laser operating at  $\lambda = 632.8$  nm was utilized as an excitation source. The Rayleigh line was removed from the collected Raman data by placing a holographic notch filter in the collection path. A charge coupled device camera was coupled to a spectrograph to provide a combined spectral resolution of  $1 \text{ cm}^{-1}$ . SERS mapping images were obtained using a Raman point-mapping method with a  $20 \times$  objective lens, the laser spot size was 1.93  $\mu\text{m}$ . Baseline correction of each Raman spectrum was performed using Renishaw WIRE 4.0 software.

**Numerical Simulations:** The numerical simulations were performed with COMSOL Multiphysics 5.3. The structures were first sketched using Autodesk Fusion 360 and then imported them into COMSOL Multiphysics. A linearly polarized plane wave with the wavelength of the excitation (632.8 nm) was incident directly upon the plasmonic nanostructures with polarization along the dimer axis. In the simulations, the permittivity of gold was set to  $\epsilon_{\text{Au}} = -11.740 + 1.2611i$ .<sup>[31]</sup> The refractive indexes of PET and the antibody were taken as 1.636 and 1.450, respectively.<sup>[32]</sup>

## Supporting Information

Supporting Information is available from the Wiley Online Library or from the author.

## Acknowledgements

X.W. and S.-G.P. contributed equally to this work. The National Research Foundation of Korea supported this work (K20904000004-12A0500-00410). This work was supported from the Korea Institute of Planning and Evaluation for Technology in Food, Agriculture, and Forestry (IPET) through the Advanced Production Technology Development Program funded by Ministry of Agriculture, Food and Rural Affairs (MAFRA-316080-04). This work was also supported by the Fundamental Research Program (PNK 5510) of the Korean Institute of Materials Science (KIMS). X.X. was supported by Lee Family Scholars. S.A. Maier

acknowledges ONR Global and the EPSRC Reactive Plasmonics Programme (EP/M013812/1), and the Lee-Lucas Chair in Physics.

## Conflict of Interest

The authors declare no conflict of interest.

## Keywords

multiplex detection, mycotoxin, reproducibility, SERS imaging, SERS mapping

Received: April 28, 2018

Revised: June 19, 2018

Published online:

- [1] L. Anfossi, C. Giovannoli, C. Baggiani, *Curr. Opin. Biotechnol.* **2016**, *37*, 120.
- [2] F. Wu, J. D. Groopman, J. J. Pestka, *Ann. Rev. Food Sci. Technol.* **2014**, *5*, 351.
- [3] H. O. Arola, A. Tullila, H. Kiljunen, K. Campbell, H. Siitara, T. K. Nevanen, *Anal. Chem.* **2016**, *88*, 2446.
- [4] R. Chauhan, J. Singh, T. Sachdev, T. Basu, B. D. Malhotra, *Biosens. Bioelectron.* **2016**, *81*, 532.
- [5] J. Zhou, J. J. Xu, B. F. Huang, Z. X. Cai, Y. P. Ren, *J. Sep. Sci.* **2017**, *40*, 2141.
- [6] B. P. Y. Lau, P. M. Scott, D. A. Lewis, S. R. Kanhere, C. Cleroux, V. A. Roscoe, *J. Chromatogr. A* **2003**, *998*, 119.
- [7] I. R. Pizzutti, A. de Kok, C. D. Cardoso, B. Reichert, M. de Kroon, W. Wind, L. W. Righi, R. C. da Silva, *J. Chromatogr. A* **2012**, *1251*, 16.
- [8] Z. Y. Wang, S. F. Zong, L. Wu, D. Zhu, Y. P. Cui, *Chem. Rev.* **2017**, *117*, 7910.
- [9] Z. Y. Cheng, N. Choi, R. Wang, S. Lee, K. C. Moon, S. Y. Yoon, L. X. Chen, J. Choo, *ACS Nano* **2017**, *11*, 4926.
- [10] J. Zhou, Q. Xiong, J. Ma, J. Ren, P. B. Messersmith, P. Chen, H. Duan, *ACS Nano* **2016**, *10*, 11066.
- [11] S. M. Nie, S. R. Emory, *Science* **1997**, *275*, 1102.
- [12] M. M. Harper, K. S. McKeating, K. Faulds, *Phys. Chem. Chem. Phys.* **2013**, *15*, 5312.
- [13] R. Wang, H. Chon, S. Lee, Z. Y. Cheng, S. H. Hong, Y. Yoon, J. Choo, *ACS Appl. Mater. Interfaces* **2016**, *8*, 10665.
- [14] M. Li, S. K. Cushing, J. Zhang, S. Suri, R. Evans, W. P. Petros, L. F. Gibson, D. Ma, Y. Liu, N. Wu, *ACS Nano* **2013**, *7*, 4967.
- [15] J. Ye, Y. Chen, Z. Liu, *Angew. Chem., Int. Ed.* **2015**, *54*, 1144.
- [16] L. A. Lane, X. M. Qian, S. M. Nie, *Chem. Rev.* **2015**, *115*, 10489.
- [17] H. Y. Wang, Y. F. Zhou, X. X. Jiang, B. Sun, Y. Zhu, H. Wang, Y. Y. Su, Y. He, *Angew. Chem., Int. Ed.* **2015**, *54*, 5132.
- [18] H. Y. Wang, X. X. Jiang, S. T. Lee, Y. He, *Small* **2014**, *10*, 4455.
- [19] C. H. Zhu, G. W. Meng, P. Zhane, Q. Huang, Z. B. Li, X. Y. Hu, X. J. Wang, Z. L. Huang, F. D. Li, N. Q. Wu, *Adv. Mater.* **2016**, *28*, 4871.
- [20] J. Yang, M. Palla, F. M. Bosco, T. Rindzevicius, T. S. alstrom, M. S. Schmidt, A. Boisen, J. Ju, Q. Lin, *ACS Nano* **2013**, *7*, 5350.
- [21] C. Catala, B. Mir-Simon, X. T. Feng, C. Cardozo, N. Pazos-Perez, E. Pazos, S. G. Pedro, L. Guerrini, A. Soriano, J. Vila, F. Marco, E. Garcia-Rico, R. A. Alvarez-Puebla, *Adv. Mater. Technologies* **2016**, *1*, 1600163.
- [22] M. Lee, S. Lee, J. Lee, H. Lim, G. H. Seong, E. K. Lee, S. I. Chang, C. H. Oh, J. Choo, *Biosens. Bioelectron.* **2011**, *26*, 2135.
- [23] Z. Y. Jiang, X. X. Jiang, S. Su, X. P. Wei, S. T. Lee, Y. He, *Appl. Phys. Lett.* **2012**, *100*, 203104.

- [24] S. Lee, H. Chon, J. Lee, J. Ko, B. H. Chung, D. W. Lim, J. Choo, *Biosens. Bioelectron.* **2014**, *51*, 238.
- [25] S. M. Tabakman, L. Lau, J. T. Robinson, J. Price, S. P. Sherlock, H. L. Wang, B. Zhang, Z. Chen, S. Tangsombatvisit, J. A. Jarrell, P. J. Utz, H. J. Dai, *Nat. Commun.* **2011**, *2*, 466.
- [26] S. G. Park, C. W. Mun, X. Xiao, A. Braun, S. Kim, V. Giannini, S. A. Maier, D. H. Kim, *Adv. Funct. Mater.* **2017**, *27*, 1703376.
- [27] J. Yun, W. Wang, S. M. Kim, T. S. Bae, S. Lee, D. Kim, G. H. Lee, H. S. Lee, M. Song, *Energy Environ. Sci.* **2015**, *8*, 932.
- [28] E. C. Le Ru, E. Blackie, M. Meyer, P. G. Etchegoin, *J. Phys. Chem. C* **2007**, *111*, 13794.
- [29] Z. Huang, G. Meng, Q. Huang, Y. Yang, C. Zhu, C. Tang, *Adv. Mater.* **2010**, *22*, 4136.
- [30] N. G. Bastus, J. Comenge, V. Puntès, *Langmuir* **2011**, *27*, 11098.
- [31] P. B. Johnson, R. W. Christy, *Phys. Rev. B* **1972**, *6*, 4370.
- [32] C. J. Huang, J. Dostalek, A. Sessitsch, W. Knoll, *Anal. Chem.* **2011**, *83*.